

# Exciton transport in thin-film cyanine dye J-aggregates

Stéphanie Valleau,<sup>1,\*</sup> Semion K. Saikin,<sup>1</sup> Man-Hong Yung,<sup>1</sup> and Alán Aspuru Guzik<sup>1,†</sup>

<sup>1</sup>*Department of Chemistry and Chemical Biology, Harvard University, Cambridge, Massachusetts 02138, USA*

We present a theoretical model for the study of exciton dynamics in J-aggregated monolayers of fluorescent dyes. The excitonic evolution is described by a Monte-Carlo wave function approach which allows for a unified description of the quantum (ballistic) and classical (diffusive) propagation of an exciton on a lattice in different parameter regimes. The transition between the ballistic and diffusive regime is controlled by static and dynamic disorder. As an example, the model is applied to three cyanine dye J-aggregates: TC, TDBC, and U3. Each of the molecule-specific structure and excitation parameters are estimated using time-dependent density functional theory. The exciton diffusion coefficients are calculated and analyzed for different degrees of film disorder and are correlated to the physical properties and the structural arrangement of molecules in the aggregates. Further, exciton transport is anisotropic and dependent on the initial exciton energy. The upper-bound estimation of the exciton diffusion length in the TDBC thin-film J-aggregate is of the order of hundreds of nanometers, which is in good qualitative agreement with the diffusion length estimated from experiments.

## I. INTRODUCTION

In organic materials, excitons, quasiparticles of bound electron-hole pairs, act as the intermediates between light (photons) and charge (electrons and hole). Understanding which physical properties make certain molecular aggregates optimal for exciton transfer is one of the main current technological goals in organic material research.

In this article, we develop a computational model and employ it to explore excitonic energy transport in a particular class of organic materials: cyanine dye J-aggregates.

Discovered over 50 years ago [1, 2], J-aggregates are typically formed by organic fluorescent dye molecules and can be identified spectroscopically by the narrowing and bathochromic shift (J-band) of the lowest electronic excitation relative to the monomer band [3, 4]. These structures are characterized by the unique properties associated with their J-band: a large absorption cross-section, short radiative lifetimes, a small Stokes shift of the fluorescence line and efficient energy transfer within the aggregate [3], which can be used for designing state-of-the-art photonic devices.

J-aggregates have been studied both experimentally [5–10] and theoretically [11–15] and their applications range from being used as “reporter molecules” in mitochondrial membrane potentials in living cells [16], to photosensitizing silver halides in photography [17]. Moreover, J-aggregates are employed in dye-sensitized organic solar cells which provide several advantages over inorganic solar cells [18, 19]. Recently, cyanine dye J-aggregates have been combined with optical cavities [20–22] or coupled to quantum dots [23, 24] to form hybrid systems.

However, the current understanding of exciton transport properties, even for the most ordered J-aggregates, is rather limited. This limitation arises from the challenges encountered in the experimental characterization of their structure [3] and from the lack of information on the dissipation processes. In an effort to overcome these difficulties, the aim of

our study is to provide a theoretical model, with a minimal number of phenomenological parameters, which is useful for the determination of the J-aggregate structure and able to describe the exciton dynamics in hybrid excitonic-photonic and excitonic-electronic devices.

J-aggregates can be found in various structural arrangements including one-dimensional, planar and cylindrical [3] aggregates each exhibiting different optical and exciton energy transfer properties [25–27]. The structure of liquid-crystal cyanine dyes was initially studied using absorption and fluorescence spectroscopy by Scheibe and Kandler [28], and more recently using X-Ray diffraction and NMR by Harrison et al. [29, 30]. Nonetheless, the packing structure of J-aggregates remains unknown [3]. Different theoretical packing models for two-dimensional arrays of these pseudocyanine dye (PIC) aggregates have been proposed by Nakahara and Kuhn [31]. In this study we focus on modeling the exciton transport properties of two-dimensional (2D) thin-films using cyanine dye J-aggregates such as those realized experimentally in Ref. [32]. These highly efficient light absorbing thin-films are employed in various opto-electronic systems for applications such as lasers and optical switches [33–35]. Exciton dynamics in these films, in general, possesses both ballistic (quantum) and diffusive (classical) regimes and can be analyzed at different levels of approximation.

Experimentally, transport properties, such as diffusion coefficients of excitons in organic materials can be obtained using indirect methods only. These include exciton-exciton annihilation [10, 22, 36], photoluminescence quenching [37, 38], transient grating [39] and photocurrent response [40, 41]. In a recent study by Akselrod et. al. [22] the singlet exciton diffusion length in a 2D cyanine dye film has been estimated to be of the order of 50 nm at room temperature which is more than twice larger than the diffusion length measured in standard organic semiconductor films [38].

Theoretically, exciton transport has been studied using a classical hopping model [42]. However, this approach is applicable only in the weak Förster coupling regime [43], where the exciton mobility is low. Beyond this regime, the tight-binding Hamiltonian with classical noise model, proposed in the 70’s by Haken, Strobl, and Reineker [44, 45] allows for a unified description of ballistic and diffusive exciton dynam-

\* [svalleau@fas.harvard.edu](mailto:svalleau@fas.harvard.edu)

† [aspuru@chemistry.harvard.edu](mailto:aspuru@chemistry.harvard.edu)

ics. For perfect structures with translational symmetry this model can provide analytic solutions for the moments of the exciton wave function [46] that characterize exciton transport. Variations of this type of analysis have been provided by others [47–51]. Incorporating a detailed computational ab-initio approach into this model increases its accuracy by providing more insight on the specific characteristics of exciton transport and by removing the limitation on the structural symmetry.

To demonstrate the applicability of our model, we present a detailed study of exciton diffusion in three types of cyanine-dye J-aggregates, namely TC (5,5'-dichloro-3,3'-disulfopropyl thiocyanine), TDBC (5,6-dichloro-2[3-[5,6-dichloro-1-ethyl-3-(3-sulfopropyl)-2(3H)-benzimidazolide]-1-propenyl]-1-ethyl-3-(3-sulfopropyl) benzimidazolium hydroxide), and U3 (3-[(2Z)-5-chloro-2-[[[(3E)-3-[[5-chloro-3-(3-triethylammonium-sulfonatopropyl)-1,3-benzothiazol-3-ium-2-yl]methylene]-2,5,5-trimethylcyclohex-1-en-1-yl)]methylene]-1,3-benzothiazol-3(2H)-yl] propane-1-sulfonate). The developed theoretical model provides a tool for the analysis of transport properties and can be utilized in modeling hybrid excitonic-photonic devices.

Our findings indicate anisotropy in the exciton diffusion, the presence of coherent dynamics at times shorter than tens of femtoseconds and finally a dependence of transport on the specific molecular excitation parameters.

The paper is organized as follows. In Section II, we describe the theoretical model for the exciton dynamics. In particular, we introduce the Hamiltonian of the system and the associated Langevin equation. The static and dynamic noises, which represent the different types of disorder present in J-aggregate films, are discussed. The description of the model is completed with a derivation of the diffusion equation. Section III includes details of the calculation of the Hamiltonian's parameters and also gives an overview of the Monte-Carlo Wave Function method (MCWF) employed in the study of exciton propagation. In Section IV we analyze exciton transport in thin-film J-aggregates of three different cyanine dyes: TC, TDBC, and U3 (structures are shown in Fig. 1). We conclude the study by summarizing our results in Section V.

## II. THE MODEL

### A. Hamiltonian and single exciton dynamics

We apply the general exciton theory developed previously for molecular crystals and molecular aggregates [52, 53] to a specific system - a 2D monolayer J-aggregate of fluorescent dye molecules. The exciton Hamiltonian of a 2D aggregate can be constructed starting from that of single monomers by explicitly incorporating intermolecular couplings. The multi-exciton space of the aggregate consists of independent exciton manifolds that are defined by a specific number of excitations in the system. The manifolds are coupled to each other by exciton relaxation, annihilation or creation processes. A more detailed discussion on the single-molecule Hamilto-

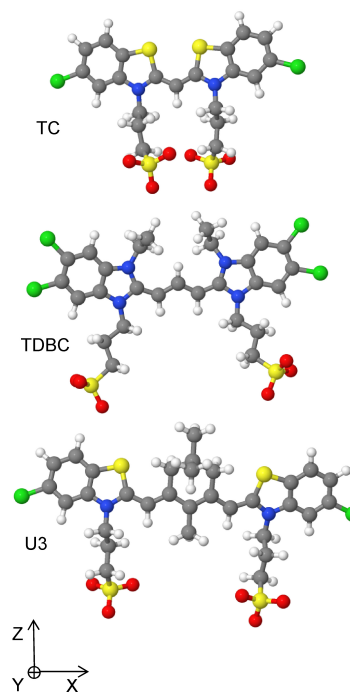


Figure 1. Structure of the monomer dye molecules TC, TDBC, and U3 which form the aggregates. The full IUPAC names of the molecules are given in the text.

nian and the exciton-manifolds is provided in Appendices A and B. Here we constrain the exciton dynamics to the single-exciton manifold and therefore assume that the exciton density of the system is low. The Hamiltonian for a single exciton in a molecular aggregate can be written as

$$\hat{H} = \hat{H}^{\text{el}} + \hat{V}^{\text{el-bath}} + \hat{H}^{\text{bath}}, \quad (1)$$

where  $\hat{H}^{\text{el}}$  is the system Hamiltonian which includes the electronic degrees of freedom,  $\hat{V}^{\text{el-bath}}$  is the system-bath interaction Hamiltonian and  $\hat{H}^{\text{bath}}$  is the bath Hamiltonian. The electronic Hamiltonian in the site basis can be expressed as

$$\hat{H}^{\text{el}} = \sum_{n=1}^N \epsilon_n |n\rangle \langle n| + \frac{1}{2} \sum_{n,m=1}^N J_{nm} |n\rangle \langle m|, \quad (2)$$

where  $\epsilon_n$  are the energies of the electronic excitations at each site  $n$  and  $J_{nm}$  are the couplings between electronic transitions of monomers at sites  $n$  and  $m$ , for an aggregate of  $N$  monomers. The energies  $\epsilon_n$  are assumed to be equal for all sites and disorder in these diagonal energies will be included as described in Section II B. In Eq. 2,  $|n\rangle = |0\dots 1_n \dots 0\rangle$  corresponds to the state where an exciton is localized at the  $n$ -th molecule and all other molecules are in their ground electronic state. In the aggregate, each monomer is modeled as a two level system and the environment is assumed to be a harmonic bath formed by the intra and intermolecular vibrations

$$\hat{H}^{\text{bath}} = \sum_n \sum_q \omega_q \hat{b}_{qn}^\dagger \hat{b}_{qn}, \quad (3)$$

where  $q$  runs over all vibrational modes. The system-bath interaction term in the linear coupling limit is

$$\hat{V}^{\text{el-bath}} = \sum_n |n\rangle \langle n| \sum_q \kappa_q (\hat{b}_{qn}^\dagger + \hat{b}_{qn}), \quad (4)$$

where  $\hat{b}_{nq}^\dagger$  and  $\hat{b}_{nq}$  are the (bosonic) creation and annihilation operators for the bath modes at site  $n$  and  $\kappa_q$  is the coupling constant between the  $q$ -th vibrational mode and the electronic system, assumed to be equal for all sites.

In general, there are two possible contributions to the coupling terms: Dexter [54] and Förster interaction [43]. If the wave-function overlap between interacting molecules is not negligible, the Dexter interaction may give a significant contribution to the  $J_{nm}$  coupling term. While this term is dominant for triplet exciton transport, singlet exciton transport can be accounted for mostly by Förster coupling. Therefore, in this case, the major contribution to the  $J_{nm}$  coupling terms in Eq. 2 is due to the Förster interaction. For a pair of molecules  $m$  and  $n$ , it is given by

$$J_{nm}^{\text{F}} = \frac{1}{4\pi\epsilon_0\epsilon} \int d\mathbf{r}_1 \int d\mathbf{r}_2 \langle \phi_{ng} | \mathbf{r}_1 \rangle \langle \phi_{me} | \mathbf{r}_2 \rangle \times \frac{1}{|\mathbf{r}_1 - \mathbf{r}_2|} \langle \mathbf{r}_1 | \phi_{ne} \rangle \langle \mathbf{r}_2 | \phi_{mg} \rangle, \quad (5)$$

where  $\langle \mathbf{r} | \phi_{ng} \rangle$  and  $\langle \mathbf{r} | \phi_{ne} \rangle$  are respectively the electron wave functions of the ground and excited states of the  $n$ -th molecule in coordinate space,  $\epsilon_0$  is the vacuum permittivity and  $\epsilon$  is the permittivity of the medium. In the following discussion, we will assume  $\epsilon = 1$ . In practice, numerical calculations of the Förster term using Eq. 5 can be computationally heavy, especially for large structures. For J-aggregates, where the distance between stacked molecules is comparable to the spatial extent of each molecule, it is possible to use the extended dipole model [55]. Within this model, the Förster interaction between two particular electronic transitions is parametrized by a transition charge,  $q$ , and a transition dipole length  $l$ . The interaction term can therefore be simplified and written as a sum of Coulomb interactions between the transition charges located on different molecules,

$$J_{nm}^{\text{F}} = \frac{q^2}{4\pi\epsilon_0\epsilon} \left( \frac{1}{r_{nm}^{++}} + \frac{1}{r_{nm}^{--}} - \frac{1}{r_{nm}^{+-}} - \frac{1}{r_{nm}^{-+}} \right) \quad (6)$$

where  $r_{nm}^{+-}$  is the distance between the charge  $+q$  located on the  $n$ -th molecule and the charge  $-q$  located on the  $m$ -th molecule.

Fluorescent dyes may self-aggregate in a number of different structures [56]. When dealing with two dimensional films of cyanine dye aggregates, the brickstone model is one of most commonly employed models which can account for the experimentally observed optical properties of these aggregates. Therefore, in our work, the molecular arrangement

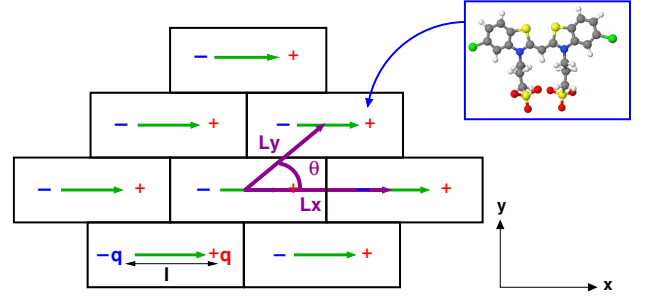


Figure 2. Brickstone lattice of a 2D J-aggregate. Each brick represents a molecule. Green arrows indicate extended molecular transition dipoles and  $l$  their length. The three lattice parameters are  $\theta$ ,  $L_x$  and  $L_y$  which can be identified by the lattice vectors  $\mathbf{L}_x$  and  $\mathbf{L}_y$ .

within the 2D layer is modeled as a brickstone lattice [7], as shown schematically in Fig. 2.

In this model, the dye molecules are stacked parallel to each other and subsequent rows are displaced by an angle  $\theta$ . The lattice is characterized by two lattice vectors  $\mathbf{L}_x$  and  $\mathbf{L}_y$ . Given the Hamiltonian of the system, we proceed to derive an equation for the quantum evolution of the system's wave function on this lattice.

The quantum dynamics of excitons can be numerically simulated using various methods, including density matrix evolution schemes [57, 58] and also diffusion [59, 60] and quantum jump [61, 62] wavefunction approaches. The latter are based on propagating the system's wavefunction rather than the density matrix and are therefore computationally more convenient to be employed for modeling large systems.

We define a quantum stochastic equation following the Langevin procedure, as described in Ref. [63]. Before including any source of noise or relaxation, the equation of motion for a single exciton in the aggregate is simply the Schrödinger equation

$$\frac{\partial |\psi(t)\rangle}{\partial t} = -\frac{i}{\hbar} \hat{H}^{\text{el}} |\psi(t)\rangle \quad (7)$$

where  $|\psi(t)\rangle$  is an exciton wave function in the single exciton manifold and  $\hat{H}^{\text{el}}$  is defined in Eq. 2. The initially excited exciton state will eventually decay back to the ground state due to interaction with the environment. Processes such as population relaxation and dephasing between excited states and the ground state can be included as follows

$$\frac{\partial |\psi(t)\rangle}{\partial t} = \left( -\frac{i}{\hbar} \hat{H}^{\text{eff}} + \sum_{m,\mu} \eta_m^\mu(t) \hat{C}_m^\mu \right) |\psi(t)\rangle, \quad (8)$$

where the effective Hamiltonian  $\hat{H}^{\text{eff}} = \hat{H}^{\text{el}} - \frac{i\hbar}{2} \sum_{m,\mu} (\hat{C}_m^\mu)^\dagger \hat{C}_m^\mu$  includes a decay term and a stochastic fluctuation term  $\eta_m^\mu(t)$  for site  $m$  and channel  $\mu$  which represents a dynamic noise force and is introduced to conserve the norm of the wave function. The  $\hat{C}_m^\mu$  are Lindblad operators

for two channels  $\mu \in \{\lambda, \phi\}$  (relaxation or dephasing) for each site  $m$ . In our case, these terms can be expressed as

$$\begin{aligned}\hat{C}_m^\lambda &= \sqrt{\Gamma^\lambda} |0\rangle \langle m| \\ \hat{C}_m^\phi &= \sqrt{\Gamma^\phi} \left( \sum_{k \neq m} |k\rangle \langle k| - |m\rangle \langle m| \right).\end{aligned}\quad (9)$$

where  $\hat{C}_m^\lambda$  describes single exciton relaxation and  $\hat{C}_m^\phi$  is introduced for dephasing processes, which are associated with the relaxation  $\Gamma^\lambda$  and dephasing  $\Gamma^\phi$  rates. The states  $|m\rangle$  span over the single exciton manifold, and the state  $|0\rangle$  denotes the ground state, where no exciton is present. The relaxation and dephasing rates are taken to be equal for all sites, because the aggregate is constructed of identical molecules which are assumed to be in identical local environments. It is easy to see that with the noise operators written in the site basis this model is equivalent to the Haken, Strobl and Reineker model [44].

### B. Static and dynamic noise

The environmental noise of the open quantum system needs to be introduced into this J-aggregate model in its various manifestations. These include fluctuations of site energies and of the site-to-site couplings as well as a term which induces exciton relaxation. When studying transport properties within the single exciton manifold, one is mostly interested in the dynamics occurring on a timescale sufficiently shorter than the exciton relaxation time, this corresponds to saying that over the time scale of the dynamics, in Eq. 10,  $\hat{C}_m^\lambda \sim 0$ . Thus, the exciton number can be assumed to be constant. Moreover, for the sake of simplicity in the provided examples we do not consider fluctuations of intermolecular interactions. Although these fluctuations can give a noticeable contribution to the transport properties [47] the main effect of noise can be captured by the fluctuations of the sole site energies.

Fluctuations of site energies can originate from low-frequency intramolecular vibrations, molecular conformations, binding and un-binding events, or charge fluctuations in a substrate or solvent which couples locally to the electronic states of molecules. Such fluctuations have been successfully modeled in natural molecular aggregates using molecular dynamics methods [64, 65]. Detailed studies of the physical origin of this noise is beyond the scope of the current paper. Here, we only emphasize that one can introduce a distinction between static and dynamic noise based on the correlation time characterizing the fluctuations as compared to the exciton propagation time. For instance if the conformation of a molecule changes on a nanosecond timescale, the fluctuation of the site energy remains correlated during the lifetime of an exciton which is of the order of tens of picoseconds. Therefore, each exciton sees different, yet static local fluctuations. In contrast, dynamic noise requires instantaneous fluctuations of the site energy with a shorter correlation time, that is in a timescale smaller or comparable to that of the energy transfer process.

Static noise can be accounted for in the Hamiltonian, Eq. 2, by introducing random shifts in the site energies. In our model, we extract the random shifts from a Gaussian distribution

$$f(\epsilon_n - \epsilon_0) = \frac{1}{\sqrt{2\pi\sigma^2}} e^{-(\epsilon_n - \epsilon_0)^2/2\sigma^2} \quad (10)$$

where  $\sigma$  is the variance, and  $\epsilon_0$  is the transition energy of each isolated molecule. The static noise distribution is assumed to be identical for all monomers. Other choices of static disorder models are possible. For instance, a more general Levy distribution can be used, which results in different state distributions and optical properties [66].

Dynamic noise directly enters the Schrödinger-Langevin equation, Eq. 8 described in the previous section. The requirement that the norm of  $|\psi(t)\rangle$  is preserved imposes certain properties on the dynamic noise force  $\eta(t)$  [63]. First, the average of  $\eta(t)$  should vanish, i.e.,  $\langle \eta(t) \rangle = 0$ . Otherwise, one has to renormalize the unperturbed Hamiltonian in Eq. 2 to include the noise-induced energy shifts. Second, the stochastic force  $\eta(t)$ , which is a result of multiple uncorrelated microscopic movements of the molecules constituting the aggregate lattice, does not have memory, i.e.,  $\langle \eta(t)\eta(t') \rangle \propto \Gamma^\phi \delta(t - t')$ . This corresponds to the Markov approximation, in the sense that the system-bath interaction is assumed to be quasi instantaneous and successive interaction events are not correlated. In general, the Markov approximation holds, as long as the bath correlation time is much smaller than the time over which one extracts properties of the system. Therefore it is only necessary that the bath correlator be sharply peaked [63, 67]. Within this argumentation the dynamic noise can be characterized by a single parameter  $\Gamma^\phi$ , which describes both the bath dynamics and the system-bath coupling. While avoiding a detailed description of the specific environment of a J-aggregate we can make the rather qualitative assumption that  $\Gamma^\phi$  is of the order of  $k_B T$ . Such assumption is not strictly justified but can be intuitively explained as following.

If we assume that the bath modes can be modeled as a set of harmonic oscillators, we can define, within linear response theory, a system bath interaction term linear in the displacement of the bath modes. It follows that the bath correlator can be expressed as [68]

$$\begin{aligned}\langle \eta(\tau)\eta(0) \rangle &= \sum_q |\kappa_q|^2 \langle (\hat{b}_q^\dagger(\tau) + \hat{b}_q(\tau)) (\hat{b}_q^\dagger(0) + \hat{b}_q(0)) \rangle \\ &= \int d\omega J(\omega) \left[ \coth\left(\frac{\hbar\omega\beta}{2}\right) \cos(\omega\tau) - i \sin(\omega\tau) \right]\end{aligned}\quad (11)$$

where the bath operators are given in the interaction picture and we have assumed that the noise correlator is the same for all sites and that each bath is uncorrelated from that of other sites. The second line corresponds to the approximation of a continuous bath spectrum with a spectral density  $J(\omega)$ . Such approximation provides a qualitative correspondence between the temperature and the dynamic noise in the system. In general, a more quantitative analysis should include explicitly the

bath vibrational modes. By using the continuous limit of the spectral density we intentionally simplified the model making it independent of the specific molecular vibrational modes. Several forms of bath spectral densities are used for modeling dissipative quantum dynamics in molecular aggregates [69–72]. We choose to employ the Ohmic exponentially cutoff spectral density  $J(\omega) = \frac{\lambda}{\hbar\omega_c}\omega e^{-\frac{\omega}{\omega_c}}$  where  $\lambda$  is the reorganization energy and  $\omega_c$  is the cutoff frequency. This spectral density can be integrated analytically in Eq. 11 and it also has been used for the simulation of exciton dynamics in natural molecular aggregates in photosynthetic systems [72, 73]. In our model, the correlator in Eq. 11 can be used only in the limit when the time dependent characteristics of exciton dynamics remain steady on timescales sufficiently longer than the bath correlation time. In this case the temperature-dependent dephasing rate can be defined as [72, 74]

$$\Gamma^\phi = 2\pi \frac{k_B T}{\hbar} \frac{\lambda}{\hbar\omega_c}, \quad (12)$$

where physical properties of the bath and the system-bath coupling are introduced through the slope of the spectral density at zero frequency  $\frac{dJ(\omega)}{d\omega}|_{\omega=0} = \frac{\lambda}{\hbar\omega_c}$  [71]. Eq. 12 is strictly valid for  $T \gg \frac{\hbar\omega_c}{k_B}$  [75]. If we use, for example, values of  $\omega_c = 150 \text{ cm}^{-1}$  and  $\lambda = 35 \text{ cm}^{-1}$ , typical for the analysis of quantum dynamics in photosynthetic systems [72, 76], the dephasing rate  $\Gamma^\phi \approx 1.4k_B T$ . The reorganization energy of J-aggregates is comparable to this value, for instance,  $\lambda_{\text{TDBC}} = 29 \text{ cm}^{-1}$  [77]. By setting  $\Gamma^\phi = k_B T$  we choose a lower bound for the exciton dephasing rates. For room temperature we thus have  $\Gamma^\phi \approx 26 \text{ meV}$ . In reality, there may be more sources of dissipation, and different estimates for the bath spectral density [71, 73] can give values of the dephasing rate,  $\Gamma^\phi$  which are several times larger than the value we use.

### C. Diffusion model

In this section, we consider methods for calculating the diffusion constant  $D$  from the transport properties of the excitonic system. For classical Brownian motion, it is well-known that the diffusion constant is related to the long-time limit of the second moment  $\langle (\mathbf{r}(t) - \mathbf{r}_0)^2 \rangle$  evaluated for the initial condition where the particle is localized at a single point  $\mathbf{r}_0$  in space. Explicitly, it is given by

$$D = \lim_{t \rightarrow \infty} \frac{1}{2td} \langle (\mathbf{r}(t) - \mathbf{r}_0)^2 \rangle, \quad (13)$$

where  $d$  is the dimension of the space. For excitonic systems, in the first place, we will not assume that exciton motion can be described as the motion of classical Brownian particles. Here our goal is to show that the relationship above (Eq. 13) holds even for excitonic systems where a fully quantum mechanical treatment is assumed. In other words, the non-equilibrium dynamics of an initially localized exciton can indeed tell us about the diffusion constant which describes the excitonic motion in (or near) equilibrium.

This line of reasoning was first made by Scher and Lax [78, 79] for the calculation of the conductivity in doped semiconductors. It was later applied to the calculation of the photoconductivity of organic molecular crystals [48–50] and to the bond-precolation model [80]. The method developed by Scher and Lax is based on linear response theory [81]. To apply it to the excitonic system, we will have to imagine an external perturbation which when applied, drives the motion of the excitons. This can be physically achieved, e.g. through some non-resonant coupling with an external field which creates a spatially inhomogeneous change in the local potential term in the Hamiltonian (cf Eq. 2). However, the actual implementation of this scheme is technically challenging if not impossible. Furthermore, the formalism of Scher and Lax requires the density matrix of the excitonic system to be an identity in thermal equilibrium; as pointed out in Ref. [49], this may potentially lead to internal inconsistency in the mathematical derivation. To avoid these complications, in the following, we will present a simpler way to obtain the relationship Eq. 13 for excitonic systems, without invoking linear response theory. This approach is essentially the quantum extension of the classical approach described in Ref. [82].

To get started, we consider a dilute system of excitons where their reciprocal interaction can be ignored. We will trace the motion of a “tagged” exciton. The probability  $P(\mathbf{r}, t)$  of finding that exciton at location  $\mathbf{r}$  and time  $t$  is given by  $P(\mathbf{r}, t) = \text{Tr}[|\mathbf{r}\rangle\langle\mathbf{r}|\hat{\rho}(t)]$ , where  $\hat{\rho}(t)$  is the density matrix of the total system (i.e. exciton plus the bath) at time  $t$ . Using the following identity

$$|\mathbf{r}\rangle\langle\mathbf{r}| = \frac{1}{(2\pi)^d} \int_{-\infty}^{\infty} d\mathbf{k} e^{-i\mathbf{k}\cdot(\hat{\mathbf{r}}-\mathbf{r})}, \quad (14)$$

where  $d$  is the dimension, and  $\hat{\mathbf{r}} \equiv \sum_{\mathbf{r}'} \mathbf{r}' |\mathbf{r}'\rangle\langle\mathbf{r}'|$  is the position operator for the exciton, we write the probability of finding the exciton as

$$P(\mathbf{r}, t) = \frac{1}{(2\pi)^d} \int_{-\infty}^{\infty} d\mathbf{k} e^{i\mathbf{k}\cdot\mathbf{r}} \tilde{P}_k(t), \quad (15)$$

where  $\tilde{P}_k(t) \equiv \text{Tr}[e^{-i\mathbf{k}\cdot\hat{\mathbf{r}}(t)}\hat{\rho}(0)]$ ,  $\hat{\mathbf{r}}(t) \equiv \hat{U}^\dagger(t)\hat{\mathbf{r}}\hat{U}(t)$ , where  $\hat{U}(t) = e^{-i\hat{H}t}$  and  $\hat{H}$  is defined in Eq. 1.

Since we are considering the fluctuations of the exciton in some steady-state (long-time  $t \rightarrow \infty$ ) limit, measurable physical quantities, including the diffusion constant, should not depend on the initial condition. We can therefore choose the following initial state  $\hat{\rho}(0) = \hat{\mathbb{I}}_S \otimes \hat{\rho}_B / \text{Tr}(\hat{\mathbb{I}}_S)$ , where  $\hat{\mathbb{I}}_S$  is the identity matrix for the system, i.e. the exciton, and  $\hat{\rho}_B = e^{-\beta\hat{H}^{\text{bath}}} / \text{Tr}(e^{-\beta\hat{H}^{\text{bath}}})$  is the density matrix of the bath, which is assumed to be in thermal equilibrium. Now, inserting the resolution of the identity,  $\hat{\mathbb{I}}_S = \sum_{\mathbf{r}_0} |\mathbf{r}_0\rangle\langle\mathbf{r}_0|$ , we can write  $\tilde{P}_k(t) = (1/\text{tr}(\hat{\mathbb{I}}_S)) \sum_{\mathbf{r}_0} e^{-i\mathbf{k}\cdot\mathbf{r}_0} \text{Tr}[e^{-i\mathbf{k}\cdot\Delta\hat{\mathbf{r}}(t)} |\mathbf{r}_0\rangle\langle\mathbf{r}_0| \otimes \hat{\rho}_B]$ , where  $\Delta\hat{\mathbf{r}}(t) \equiv \hat{\mathbf{r}}(t) - \mathbf{r}_0$ . Performing the cumulant expansion [63] and keeping terms up to the second-order, we obtain

$$\tilde{P}_k(t) \approx \frac{1}{\text{tr}(\hat{\mathbb{I}}_S)} \sum_{\mathbf{r}_0} e^{-i\mathbf{k}\cdot\mathbf{r}_0} e^{-(1/2)\langle[\mathbf{k}\cdot\Delta\hat{\mathbf{r}}(t)]^2\rangle_0} \quad (16)$$

where  $\langle[\mathbf{k}\cdot\Delta\hat{\mathbf{r}}(t)]^2\rangle_0 \equiv \text{Tr}\{[\mathbf{k}\cdot\Delta\hat{\mathbf{r}}(t)]^2|\mathbf{r}_0\rangle\langle\mathbf{r}_0|\otimes\rho_B\}$ . Then, we arrive at the diffusion equation

$$\frac{\partial}{\partial t} P(\mathbf{r}, t) \approx \sum_{i,j \in \{x,y,z\}} D_{ij}(t) \frac{\partial^2}{\partial r_i \partial r_j} P(\mathbf{r}, t), \quad (17)$$

where

$$D_{ij}(t) \equiv \frac{1}{2} \frac{d}{dt} \langle \Delta \hat{r}_i(t) \Delta \hat{r}_j(t) \rangle \equiv \frac{1}{2} \frac{d}{dt} M_{ij}^{(2)}(t) \quad (18)$$

is the time-dependent tensor of the diffusion coefficients. Here we have defined the second moments  $M_{ij}^{(2)}(t) \equiv \langle \Delta \hat{r}_i(t) \Delta \hat{r}_j(t) \rangle$ . In order for the diffusion coefficients  $D_{ij}(t)$  to converge in the long time limit ( $t \rightarrow \infty$ ), the right-hand side of Eq. 18 should scale at most linearly in  $t$ . This result coincides with that in Eq. 13, which is a special case of isotropic diffusion.

### III. COMPUTATIONAL DETAILS

#### A. Monomer properties

Density-functional calculations of the molecular structure and electronic excitation spectra were performed with the quantum-chemistry package Turbomole, version 5.10. [83]. Triple- $\zeta$  valence-polarization basis sets (def2-TZVP [84]) were used together with the hybrid functional of Perdew, Burke, and Ernzerhof (PBE0) [85]. Dielectric properties of the medium were accounted for by using COSMO [86] as implemented in Turbomole.

To calculate the extended dipole parameters of the fluorescent dyes, the HOMO and LUMO orbitals of the molecules were computed on a homogeneous spatial grid. The grid steps are  $dx = 0.5 \text{ \AA}$ ,  $dz = 0.5 \text{ \AA}$  in the plane of the molecular backbone, and  $dy = 0.25 \text{ \AA}$  in the direction orthogonal to the backbone. The Förster, Eq. 5 and the Dexter interactions between pairs of molecules were calculated for center-to-center displacements scanned over  $x = [-60, 60] \text{ \AA}$  and  $y = [-10, 10] \text{ \AA}$  with step size  $\Delta x = \Delta y = 0.5 \text{ \AA}$ .

#### B. Monte Carlo wave function propagation

Eq. 8 is a Markovian stochastic open quantum system equation, which is equivalent to a Lindblad master equation for the density matrix [63]. As such one can evolve single stochastic eigenfunction trajectories instead of the full density matrix, using the Markov Monte-Carlo wave function method [61].

The initial wavefunction  $|\psi(0)\rangle = |00\dots 1\dots 0\rangle$  is defined as an exciton localized at the center of the lattice (i.e., in the position  $[\frac{n_x}{2}, \frac{n_y}{2}]$ ). At time  $t + \delta t$ ,  $|\psi(t + \delta t)\rangle$  can be obtained

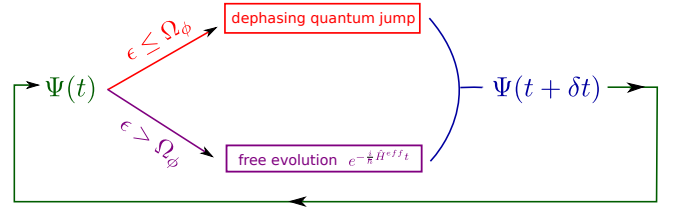


Figure 3. Monte Carlo Wavefunction stochastic dephasing jump evolution. Each stochastic trajectory  $\Psi(t)$  will evolve either by making a dephasing quantum jump or according to a non-Hermitian effective Hamiltonian  $\hat{H}^{\text{eff}}$ . The choice of making a dephasing jump is determined by a Monte-Carlo type algorithm, where one extracts a random number  $\epsilon$  and compares it to the dephasing jump probability  $\Omega_\phi$ . The procedure is repeated up to the final propagation time. One then repeats the procedure to obtain an ensemble of trajectories and average over this ensemble to obtain the desired observables.

from  $|\psi(t)\rangle$  according to the stochastic scheme depicted in Fig. 3. In particular, at each time step, if the stochastic variable extracted,  $\epsilon$ , is larger than the quantum dephasing jump probability  $\Omega_\phi$ , the wavefunction will propagate freely under the non-Hermitian effective Hamiltonian  $\hat{H}^{\text{eff}}$  introduced in Eq. 8

$$|\psi(t + \delta t)\rangle = \frac{1}{\sqrt{\mathcal{N}}} \left( 1 - \frac{i\hat{H}^{\text{eff}}\delta t}{\hbar} \right) |\psi(t)\rangle, \quad (19)$$

where  $\mathcal{N} = \sqrt{\langle \psi(t + \delta t) | \psi(t + \delta t) \rangle}$  is the normalization constant. However, if  $\epsilon$  is smaller than  $\Omega_\phi$ , a quantum dephasing jump will occur. The quantum dephasing jump, a specific type of quantum jump, is described as a flip of the sign of wavefunction's coefficient corresponding to a site  $m$  and corresponds to applying the dephasing jump operator  $\hat{C}_m^\phi$ , Eq. 9, to the wavefunction [61]. The phase jump occurs in position  $N = \text{round}(\frac{\epsilon}{\Omega_\phi} n_x n_y)$  where  $\Omega_\phi$  is defined as  $\Omega_\phi = \frac{\delta t}{2} \Gamma^\phi n_x n_y$ , and where  $\Gamma^\phi$  was given in Eq. 12 while  $\delta t$  is the time step which is assumed to be small enough so that  $\Omega_\phi \ll 1$ . For the trajectories controlled by exciton dephasing only, the effective Hamiltonian  $\hat{H}^{\text{eff}}$  is the same as  $\hat{H}_0$ , thus the norm of the wavefunction in Eq. 19 is conserved.

To analyze exciton transport properties of TC, TDBC and U3 aggregates the exciton wavefunction was propagated on a lattice of 2601 monomers ( $n_x = n_y = 51$ ) for a total time of  $t = 100 \text{ fs}$ . The quantum trajectories were averaged over 1000 different realizations of static disorder (convergence on the populations was reached with 1000 realizations within an error  $\leq 4\%$ ). The time step in the propagation was set to  $\delta t = 0.6$  as thus the probability of the quantum jump within the step is sufficiently smaller than 1, and the wave function was collected at each femtosecond. The long range interaction between the molecules has been accounted for within the cutoff distance  $l_{\text{cutoff}} = 6 \cdot L_x$ , more details about this cutoff can be found in Section IV A. The excitation was injected at the energy of the maximum of the J-band and at time zero, only the central site (26,26) of the lattice was excited. The results

were obtained in general over the range  $\Gamma^\phi = [20 - 110]$  meV and  $\sigma = [0 - 110]$  meV. Exciton diffusion coefficients were estimated from a linear fit of the second moments of the exciton distribution functions  $M_{ii}^{(2)}$ , as per Eq. 18.

## IV. RESULTS AND DISCUSSION

### A. Model Parameters

#### 1. Monomer calculations and absorption spectra

The structures of the TC, TDBC, and U3 cyanine dye molecules have been optimized using density functional theory (DFT). In the computation, we considered single-charged anions and assumed that the  $\text{Na}^+$  ions were dissociated. For each molecule, although the conjugated part of the structures remain almost planar, there are many conformations which differ slightly by the orientations of the sulphonated group side chains and are all closely spaced in energy. Examples of such conformations for the *cis*-isomers are shown in Fig. 1. The difference between the ground-state energies of *cis* and *trans*-isomers of the molecules is of the order of hundreds of meV. We have chosen *cis*-isomers as our reference structure because it is most likely that in this conformation, with the sulphonate groups pointing towards the surface and binding chemically or physically to it, that one would obtain the observed 2D monolayers [32]. For each optimized molecular structure, we computed the 100 lowest electronic excitations which fall in the energy range 2-7 eV. The computed spectra of the molecules shown in Fig. 1 are provided in Fig. 4. The strong lowest excitation can be accounted for by the HOMO to LUMO transition for more than 98%. Such transition is generally assigned to the lowest absorption peak observed in the monomer spectra of fluorescent dyes. The second electronic transition is separated from the lowest one by about 0.7 eV, 1.0 eV, and 1.4 eV for TC, TDBC and U3 respectively. Moreover, the oscillator strengths of these subsequent transitions are about two orders of magnitude smaller than that of the lowest one. These results support the two-level model provided that the static energy disorder is of the order of 100 meV. The computed frequencies of the lowest electronic transitions are systematically blue-shifted by about several hundreds of meV as compared to the experimental values. This shift typically occurs in DFT calculations with the PBE0 functional [87]. Similarly to what was found for the ground state energies, the lowest electron transition frequencies for *trans* and *cis*-isomers differ by hundreds of meV's.

#### 2. Couplings

The extended dipole parameters for the lowest electron excitation are calculated within the Frontier Orbital Approximation (FAO) [88], in which one assumes that only the HOMO-LUMO transition is involved. To obtain the  $l$  and  $q$  parameters in the extended dipole coupling formula Eq. 6, we assume that the only type of interaction involved is Förster interaction

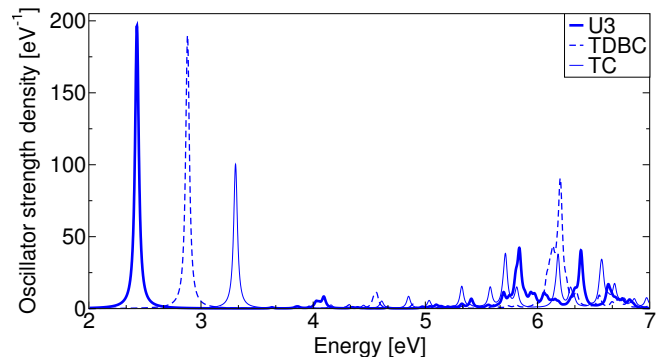


Figure 4. Computed spectra of electronic excitations in TC, TDBC, and U3 *cis*-isomers. The lines are broadened with Lorentzians of 20 meV linewidth.

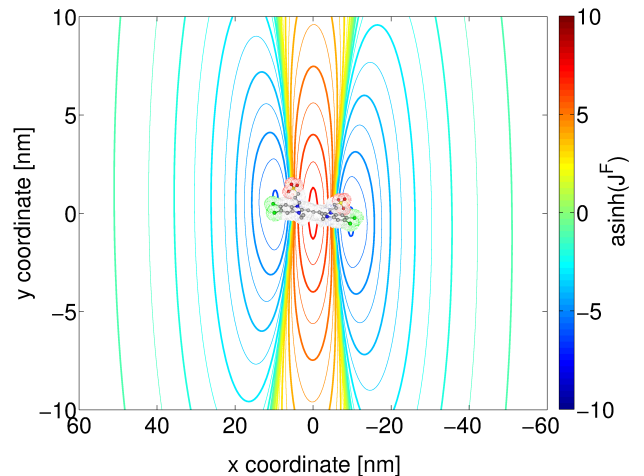


Figure 5. 2D map of the Förster interaction between two TC molecules aligned to each other. The axes show center-to-center displacement of the molecules. The inset figure shows the orientation of the long-range behaviour of the interaction. The blue-green colors define the negative frequency shift of the lowest electronic excitation, while the yellow-red colors indicate the positive shift.

(Eq. 5) and fit the interaction between two molecules on the  $x - y$  plane to the Förster results. An example of the calculated interaction contour plot for a pair of TDBC molecules is shown in Fig. 5. For intermolecular distances larger than  $2 \text{ \AA}$ , the profile reproduces the interaction of two dipoles and can easily be fitted with the extended dipole formula. The largest positive shift of the electron transition is obtained when the molecules are displaced along the  $y$ -axis (direction orthogonal to the backbone of the molecules). The largest negative shift of the electron transition corresponds to the case when molecules are displaced along the  $x$ -axis approximately by half of the length of the molecule. These results are consistent with the extended dipole model. The computed properties of TC, TDBC, and U3 monomers are summarized in Table I. We also computed Dexter couplings and these were much smaller than the corresponding Förster terms for distances of the order of the physical spacing between molecules and were therefore

Dye	$\Omega$ [eV]	$\mu$ [D]	$\mu_{\text{HL}}$ [D]	$l$ [Å]	$q$ [e]
TC	3.3	8.9	8.3	9.1	0.20
TDBC	2.9	13.1	11.0	10.5	0.22
U3	2.4	14.6	12.5	11.1	0.24

Table I. Computed excitation properties of fluorescent dye molecules.  $\Omega$  is the frequency of the electronic excitation,  $\mu$  is the transition dipole associated with the transition computed using TDDFT,  $\mu_{\text{HL}}$  is the transition dipole computed using HOMO-LUMO orbitals only,  $l$  is the length of the extended dipole, and  $q$  is the charge associated with the extended dipole.

neglected.

### 3. Lattice Parameters and absorption spectra

The brickstone lattice parameters were determined as following. The horizontal distance between monomers  $L_x = |\mathbf{L}_x|$  was chosen to be the optimized length of the molecule in the *cis*-geometry  $l_0^{\text{cis}}$  plus twice the Van der Waals radius of the chlorine atom. In particular we chose the longitudinal Van der Waals radius determined for a C-Cl type bond  $r_{\text{Cl}} = 1.58$  Å, as reported in Table 11 of [89]. The angle between monomers was set to  $\theta = \tan^{-1}\left(\frac{2L_y}{L_x}\right)$ . Having fixed  $\theta$  and  $L_x$  we then determined the vertical distance between layers of monomers  $L_y \cdot \sin\theta$  by fitting the theoretical position of the J-band in the absorption spectra to the experimental result. All of these parameters are reported in Table II

Dye	$l_0^{\text{cis}}$ [Å]	$L_x$ [Å]	$L_y \cdot \sin\theta$ [Å]	$\theta$ [rad]
TC	15.01	18.17	3.815	0.421
TDBC	17.36	20.52	4.600	0.404
U3	19.72	22.88	5.120	0.427

Table II. Lattice parameters for the three molecules.  $l_0^{\text{cis}}$  is obtained from the DFT optimization of the molecular structure,  $L_y$  parameters were obtained from fitting the theoretical spectrum to the experimental J-band shift.

The measured energies of the lowest electronic transitions for TC, TDBC and U3 dyes in solution and also in the aggregated form are collected in Table III.

Dye	Monomer transition [eV]	J-band [eV]	$\Delta$ [eV]	Ref.
TC	2.900	2.613	0.287	[90]
TDBC	2.396	2.115	0.281	[91]
U3	1.864	1.571	0.293	[92]

Table III. Experimental data for electron excitations in monomer and J-aggregated dyes as well as  $\Delta$  the shift between monomer and J-band.

To estimate the shifts of the J-band due to the molecular aggregation the excitonic spectra of the aggregates have been computed by diagonalizing the Hamiltonian, Eq. 2, for all

three dyes. The oscillator strength of a particular transition is proportional to the square of the corresponding transition dipole. To account for the static disorder the transition frequencies of the monomers were taken from a Gaussian distribution of width 70 meV. In Fig. 6 the calculated spectra of J-aggregates are shown as compared to the energies of single molecule excitations. The peak positions were fitted to the experimental results. To obtain the correct shift within 5% of error, we determined that the cut-off distance for the molecule-molecule interaction should be not smaller than  $l_{\text{cutoff}} = 6 \cdot L_x$ . We observe the typical band narrowing of the J-band whereas the exact vibrational structure of the monomer and the J-band cannot be captured with this simple analysis and is beyond the scope of the present paper. Moreover, the present analysis doesn't account for the line shift due to the non-resonant (van der Waals) interactions.

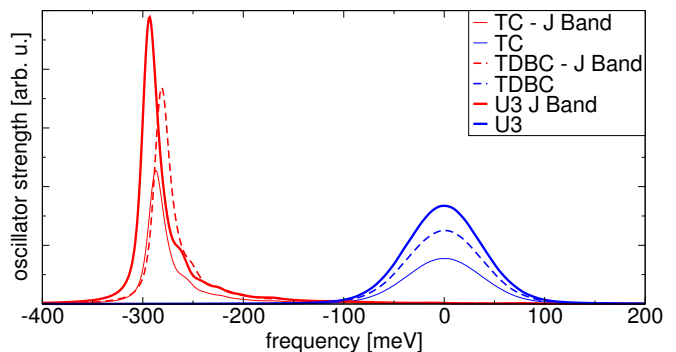


Figure 6. Calculated electronic excitation spectra of the three molecular aggregates, TC, TDBC and U3, as compared to the electronic transitions of monomers that form the aggregates. Zero frequency correspond to the energy of a monomer excitation. The transition frequencies of the monomers were taken from a Gaussian distribution of the width 70 meV to account for the static disorder.

## B. Quantum exciton dynamics

The developed model accounts for both coherent and incoherent properties of exciton dynamics that can be monitored by following the spatial distribution of the exciton population

$$P_{ij}(t) = \overline{\langle ij|\psi(t)\rangle\langle\psi(t)|ij\rangle}, \quad (20)$$

where  $(i, j)$  is the pair of cartesian indices for a particular molecule on the 2D lattice and the bar above the expression corresponds to the ensemble average over quantum trajectories. In addition, to characterize specifically the role of coherences in the exciton transport we analyze the two-point one-time correlations between the central site (the point of the exciton injection) and the current site  $(i, j)$

$$C_{ij}(t) = \overline{|\langle ij|\psi(t)\rangle\langle\psi(t)|0\rangle|}. \quad (21)$$

A similar quantity has been used previously in Refs. [93, 94] to estimate the exciton delocalization length in natural molec-



ular aggregates. If the exciton transport is completely incoherent and represented by the hopping of exciton population between sites, the correlation function, Eq. 21, should remain zero for all times provided that no initial site-site correlations were created. This is consistent with the conventional Bloch equations, where the coherence dynamics and the population dynamics are separated. In Figs. 7 and 8 we show an example of the population and coherence dynamics in TDBC J-aggregate when the dynamic disorder is  $\Gamma^\phi = 30$  meV and static disorder is  $\sigma = 70$  meV.

Based on the discussion in Section II B, this value of dynamic disorder represents a lower bound to the exciton dephasing rate (upper bound to the exciton diffusion length) at room temperature. One can see that exciton transport is anisotropic and the population spreads in time following approximately an elliptic shape with major axis  $x$  and minor axis  $y$  (such directions are indicated in Fig. 2). The population spreads about 2 to 3 times faster in the  $x$  direction than it does in the  $y$  direction. This can be explained by analyzing the direction of maximum coupling between nearest neighbors. In fact, looking at the lattice in Fig. 2 and considering the molecule placed at the origin of the purple lattice vectors, we see that it has four first nearest neighbors, one of which is indicated by the  $L_y$  vector. The sum of the nearest neighbors coupling vectors taken in pairs along the  $x$  axis is greater than that along the  $y$  axis. The fact that the exciton is transported in the direction of maximum coupling is also seen in Fig. 9 where the population is more rapidly transferred to site (26,27) along the principle  $x$  direction respect to site (24,27) which is along the  $y$  axis.

By comparing Fig. 7 to Fig. 8, we notice that coherences are spread and suppressed much more rapidly than populations. However, the principal transport axis remains the same, i.e it is the major axis of the ellipse. This is true for all examined values of static and dynamic disorder. At times shorter than about 30 fs the dynamics is coherent and interesting shapes such as a four leaved clover at 2 fs appear in the coherence plot. At longer timescales incoherent diffusion prevails and these features mostly disappear. The peaks of these correspond to beats in coherences between second to fourth nearest neighbors but such beats die off rapidly over a couple of tens of femtoseconds. While quantitative differences are observed between the molecules, the general trend is qualitatively similar to the one shown in the example. As a possible extension of this initial study of coherent dynamics it would be interesting to explore the phase directed exciton transport in these two-dimensional aggregates as has been done for the one dimensional case [95].

While the initial condition (a localized exciton) determines a rather large population of the central site even at relatively long times, this does not globally affect the exciton diffusion properties of the aggregate. Furthermore, the localized excitation can be viewed as exciton injection from a donor.

### C. Diffusion coefficient and diffusion length

The computed wave function provides the most complete source of information about the exciton dynamics. Its second moment can capture the main diffusive and ballistic features of the transport. For a homogeneous system with stochastic dephasing noise and translational invariance, the moments of the wave function in Eq. 8 can be written analytically [46]. If the exciton is initially localized on a particular molecule one should expect a ballistic exciton propagation (the second moment scales quadratically in time,  $M^{(2)} \propto t^2$ ) followed by the diffusive motion (the second moment is linear in time,  $M^{(2)} \propto t$ ). For systems with static disorder similar transport regimes should be observed provided that the dynamic noise is strong enough to overcome exciton localization. To verify this the second moments of the wave functions each trajectory were computed over an interval of 100 fs with a time step of 1 fs and averaged over a thousand trajectories. In Fig. 10 an example of  $M^{(2)}(t)$  for the TDBC J-aggregate with static disorder  $\sigma = 70$  meV and dynamic disorder  $\Gamma^\phi = 30$  meV is shown. On timescales shorter than about 30 fs the scaling of  $M^{(2)}$  is approximately quadratic, while the longer time dynamics reflects the diffusive transport. A similar tendency is observed for other molecules within the whole studied spectrum of  $\sigma$  and  $\Gamma^\phi$  with the free exciton propagation time shrinking down to below 20 fs for large values of  $\Gamma^\phi$ .

The exciton transport properties depend on the initial injection energy  $E_{in}$ . Results showing the second moment as a function of  $E_{in}$  together with the exciton density of states (DOS) are reported in Fig. 11. We see that there is a maximum in the moments somewhere between the J-band ( $E_{in} = -281$  meV) and the monomer band ( $E_{in} = 0$  meV). This is true at all times and the position of the maximum is different for the  $xx$  component than it is for the  $yy$  component. This can be correlated to the large density of states in that energy interval (Fig. 11 top panel). The high density of states is not sufficient to explain the exact position of the maximum, in fact, while the density of states has a maximum at about  $-72$  meV, the second moment is peaked at about  $-170$  meV for the  $xx$  component. The same trend in the second moments is observed for TC, and the only apparent difference is that the values of the second moment are smaller. One aspect to keep into consideration is that although there is a large density of states around  $60 - 80$  meV, these states mostly have small oscillator strengths (See Fig. 6). To investigate further the origin of the differences in these maxima one should look into the structure and spatial overlap of the exciton states.

To estimate the exciton diffusion coefficients the linear fit was taken over the time interval  $\Delta t_1 = 30 - 100$  fs to exclude the initial ballistic propagation of the exciton. For most values of static and dynamic disorder, the boundary effects associated with the finite size of the simulated lattice is negligible on the timescale of 100 fs. However, for weak dynamic noise the exciton wavefunction reaches the boundary of the simulated lattice along the  $y$ -axis at about 70 fs. In such cases the  $yy$  component of the diffusion coefficient  $D_{yy}$  was fitted on the time range  $30 - 70$  fs. With the initial condition of injection into the J-band, the diffusion coefficients were calculated

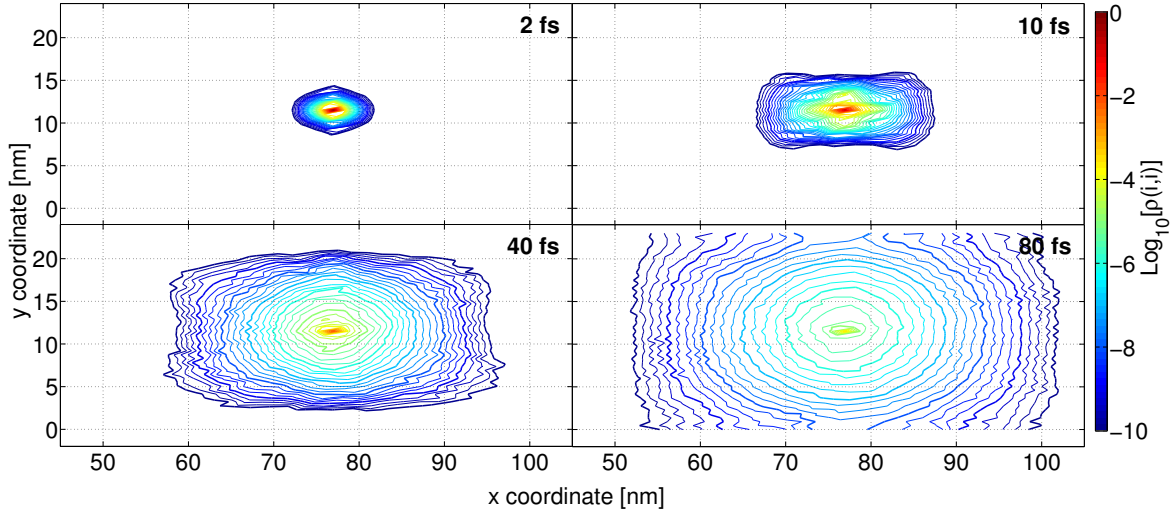


Figure 7. Contour plots of logarithm of exciton population in TDBC J-aggregate projected onto coordinate space at 2, 10, 40 and 80 fs. Here, the static disorder is  $\sigma = 70$  meV and the dynamic disorder is  $\Gamma^\phi = 30$  meV. Population spreads more rapidly in the  $x$  direction than in the  $y$  direction. This behavior is observed for all studied values of dynamic and static disorder and can be explained by the couplings between monomers as described in the text.

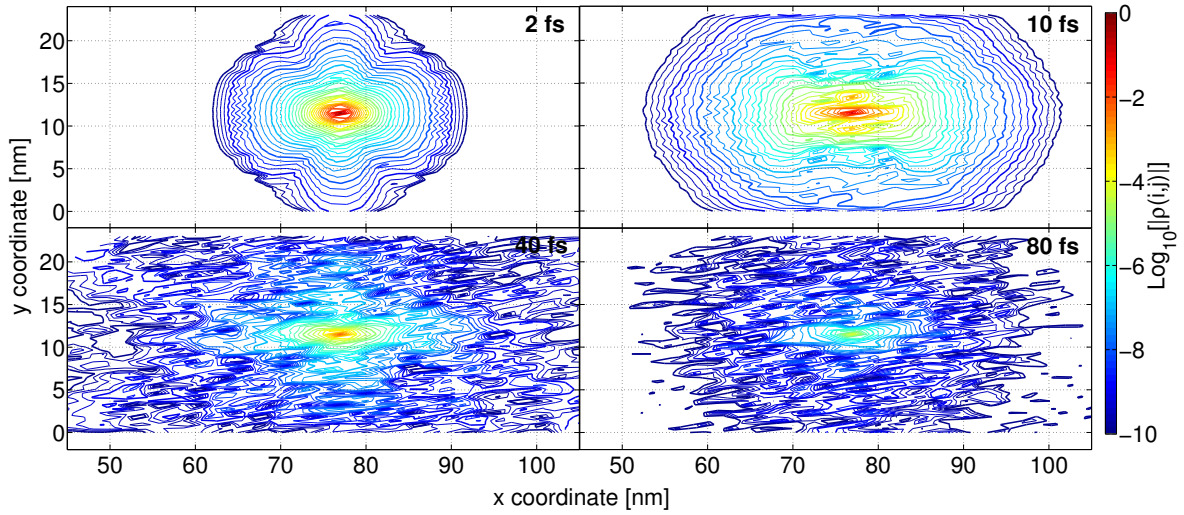


Figure 8. Contour plots of logarithm of exciton population in TDBC J-aggregate projected onto coordinate space at 2, 10, 40 and 80 fs. Here, the static disorder is  $\sigma = 70$  meV and the dynamic disorder is  $\Gamma^\phi = 30$  meV. Coherences spread more rapidly in the  $x$  direction than in the  $y$  direction. This behavior is observed for all studied values of dynamic and static disorder and can be explained by the couplings between monomers as described in the text. Further, coherences spread and decay much more rapidly than populations, as can be seen by comparing to Fig. 7.

using

$$M_{ii}^{(2)}(t) = 2D_{ii}t \quad (22)$$

for each type of aggregate. The results are shown in Fig. 12. Two distinct characteristics emerge from this plot. First of all, we notice that diffusion is greater for U3 than it is for TDBC which in turn is greater than that of the TC aggregate. This can be explained by looking at the physical characteristics of the molecules (Tab. I). U3 has the largest transition dipole, this leads to stronger coupling between the monomers and thus to

more rapid exciton density transfer. The diffusion coefficients normalized with respect to the square of the corresponding transition dipole (not shown in the figures) are similar for two molecules, TDBC and U3, while the normalized diffusion for TC is still higher. We attribute this difference to the closer packing of TC molecules. This trend is robust to both static and dynamic disorder, so long as both are finite and not so large as to lead to localization. This implies that independently of temperature, within the studied interval, the transport efficiency is dictated by the specific physical properties of the molecules. Of course, the geometric arrangement is a

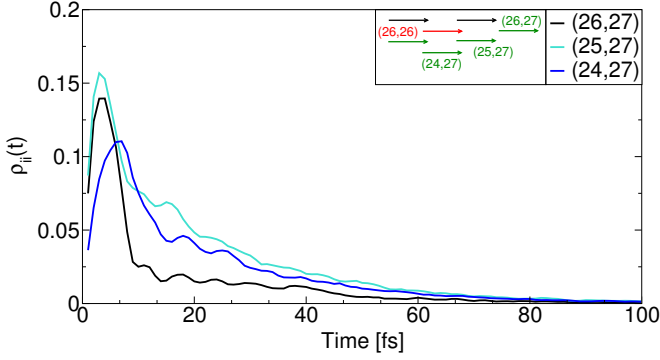


Figure 9. Populations of sites neighboring source (26,26) as a function of time for TDBC with  $\sigma = 70$  meV and  $\Gamma^\phi = 30$  meV. Population is transferred most rapidly from the central site (26,26) to site (25,27), the first nearest neighbor and then to site (26,27) which is in the direction of maximum transport.

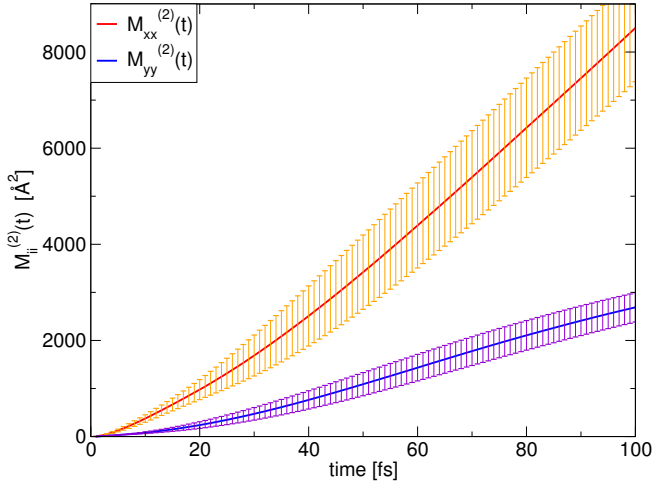


Figure 10. Second moment of the exciton wavefunction in time for TDBC aggregate with static disorder  $\sigma = 70$  meV and dynamic disorder  $\Gamma^\phi = 30$  meV. Both  $xx$  and  $yy$  components are included with their respective error bars. A transition from a ballistic regime to a diffusive regime is observed at about 30 fs. For all studied values of static and dynamic disorder these two regimes are observed and the transition is always at about 20 – 30 fs.

criteria which can alter this trend since it will explicitly modify the couplings. Then secondly, as noticed from the wavefunction propagation, diffusion is faster along the  $x$  axis than it is along the  $y$  axis. This difference is largest for small values of disorder (about a 3-fold difference) where the propagation is fastest, in the quasi ballistic regime. Going to larger disorder, the wavefunction spreads much slower and propagation is reduced in both directions.

Finally, we investigated the transport as a function of static disorder as well. The three dimensional surface plots for TC and TDBC are shown in Fig. 13. We notice that diffusion is strongly dependent on  $\Gamma^\phi$  and much less dependent on  $\sigma$ . For each fixed value of  $\Gamma^\phi$ , the largest variation of  $D_{ii}$  over the  $\sigma$  interval is of about 30% of the largest values. On the other

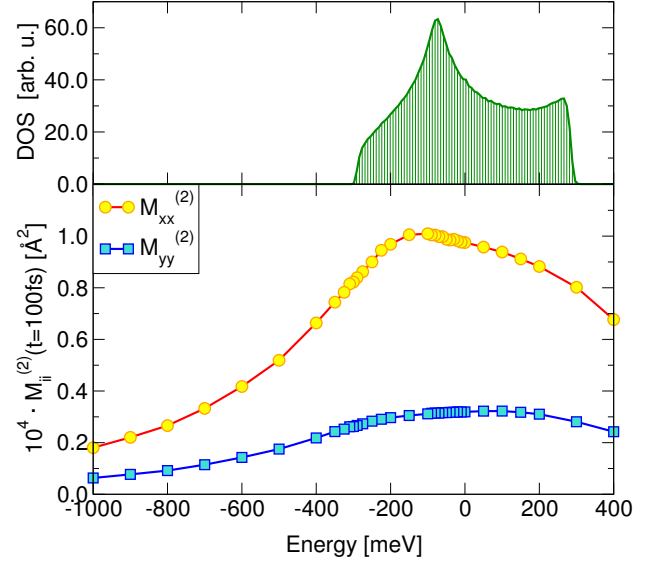


Figure 11. Top panel: Density of exciton states as a function of energy of states computed for an aggregate of 51x51 TDBC molecules and averaged over 1000 realizations of static disorder  $\sigma = 70$  meV. The zero of energy corresponds to the electronic transition of a single molecule. The energy of the central site (injection point) in the lattice is assumed to be zero. Bottom panel: Plot of second moments of the wave function at time  $t = 100$  fs as a function of the initial injection energy for TDBC with static disorder  $\sigma = 70$  meV and  $\Gamma^\phi = 30$  meV.

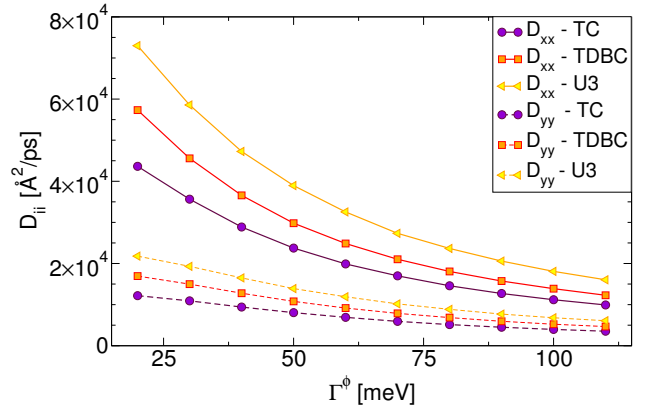


Figure 12. Comparison of diffusion constants as a function of dynamic disorder  $\Gamma^\phi$  for TC, TDBC and U3 with static disorder  $\sigma = 70$  meV. As dynamic disorder is increased, the diffusion constants decrease. Further,  $xx$  diffusion constants are larger than  $yy$  components for all values of dynamic disorder. Finally, diffusion is larger for U3 than it is for TDBC and TC. This can be explained by the molecular coupling parameters as described in the text.

hand, the largest variation of  $D_{ii}$  at fixed  $\sigma$  and varying  $\Gamma^\phi$  is of the order of 80% of the largest value. Due to the presence of static disorder the dependence of the diffusion coefficient on the dephasing rate  $\Gamma^\phi$  deviates from the conventional  $D \propto 1/\Gamma^\phi$  derived within the Haken-Strobl-Reineker model for homogeneous systems [46].

Recently, Akselrod et. al. [22], have estimated the exciton

diffusion length in thin-film J-aggregates of TDBC molecules based on an exciton-exciton annihilation experiment at room temperature. In that study, the exciton lifetime obtained from time-dependent photoluminescence was determined to be  $\tau_{\text{exp}} = 45$  ps, and an expression for three-dimensional exciton diffusion was used to determine the annihilation rate. However, the sulphonated group side chains are about 6 Å long and in addition, in the growth process a layer of polymer molecules is introduced between the J-aggregate layers. As a result the spacing between the monolayers of fluorescent dyes is several times larger than the distance between nearest neighbor molecules in a layer. Therefore we can assume that diffusion in these aggregates is two dimensional rather than three dimensional. Using a 2D model, we find that the experimental exciton diffusion length is about  $\ell_{\text{exp}} \approx 60$  nm. We can estimate the exciton diffusion length along the  $i$ -th direction using the measured lifetime and a computed diffusion coefficient as

$$\ell_i = \sqrt{2D_{ii}\tau_{\text{exp}}}. \quad (23)$$

For the value of the dynamic disorder  $\Gamma^\phi = 30$  meV, which should approximately correspond to room temperature, as discussed in Section II B, and the static disorder  $\sigma = 70$  meV we find  $\ell_x \approx 200$  nm and  $\ell_y \approx 100$  nm. These values are in a good qualitative agreement with the measured one. However, the quantitative discrepancy can be due to a number of factors such as different lattice constants of the aggregate, additional exciton dephasing and relaxation channels, and also domain boundaries in the experimental structures. All of these aspects can be incorporated into the model provided that one can extract the actual parameters should from experiments.

## V. CONCLUSIONS

In this article, a mixed model combining an open quantum systems approach to *ab-initio* calculations has been employed to gain insight on the exciton dynamics of thin-film J-aggregates. This model can capture both coherent and incoherent transport and allows for a detailed study of transport parameters such as diffusion coefficients and diffusion length. The role of the initial state of the system on transport can also be captured. Further one can investigate all these aspects as a function of the structure of the aggregates through the lattice parameters.

As an example the model was applied to three different cyanine dye aggregates. Within this model we conclude that transport depends explicitly on the molecular properties of the monomers which compose the aggregate. In particular, for molecules packed in a brickstone arrangement, transport increases with the monomers' transition dipoles and hence with the coupling between monomers. Furthermore, the coupling induces a preferential direction for transport which leads to an anisotropic spread of populations and coherences. Such directionality is robust to both static and dynamic disorder within the investigated ranges and does not change for different molecules. This model has permitted the identification

of timescales for the different transport regimes. A ballistic regime is present for all values of disorder at times smaller than 20 fs while afterwards a diffusive regime is observed. The transport is also determined by the choice of the initial condition, at a specific value of injection energy a maximum in diffusion is observed. Investigation on the origin of the exact position of this maximum are planned but qualitatively it can be explained by the large DOS located between J-band and monomer transition.

The obtained diffusion length is in good agreement with experimental results, however a more accurate comparison would be possible only including relaxation in the excited state manifold. The model does not account for exciton domains which would reduce diffusion, and further we cannot investigate the low temperature regime. Work in these directions is currently in progress in our research group.

The efficient exciton transport observed in these thin-film aggregates and the possibility of tuning this transport by the choice of monomers or by selecting the initial condition makes these aggregates good candidates for devices where large exciton diffusion lengths are sought. In particular coupling them to optical micro-cavities [96] opens the road to a range of control possibilities which we plan to study in future work. Coupling these large-exciton diffusion length materials to high-hole mobility materials [97] might also provide some advantages for technological applications such as all-organic photon detectors.

## ACKNOWLEDGMENTS

We appreciate useful discussions with G. Akselrod, D. Arias, R. Olivares-Amaya and D. Rappoport. Further the authors would especially like to thank A. Eisfeld for the many fruitful comments which greatly enriched this project.

This work was supported by the Defense Threat Reduction Agency under Contract No HDTRA1-10-1-0046. S. V. acknowledges support from the Center for Excitonics, an Energy Frontier Research Center funded by the U.S. Department of Energy, Office of Science and Office of Basic Energy Sciences under Award Number DE-SC0001088 as well as support from the Defense Advanced Research Projects Agency under award number N66001-10-1-4060. M-H. Yung also acknowledges the Croucher Foundation for support. Further, A. A.-G. is grateful for the support of the Camille and Henry Dreyfus Foundation and the Alfred P. Sloan Foundation.

## Appendix A: Single molecule Hamiltonian

In the harmonic approximation, the single-molecule electron excitation Hamiltonian can be written as

$$\hat{H}_{\text{mol}} = \sum_i \left( \Omega_i + \sum_q \omega_{iq} \hat{b}_{iq}^\dagger \hat{d}_{iq} \right) |i\rangle \langle i|, \quad (\text{A1})$$

where  $\Omega_i$  is the energy of  $i$ -th electronic transition,  $b_{iq}^\dagger$  and  $b_{iq}$  are creation and annihilation operators for the  $q$ -th vi-

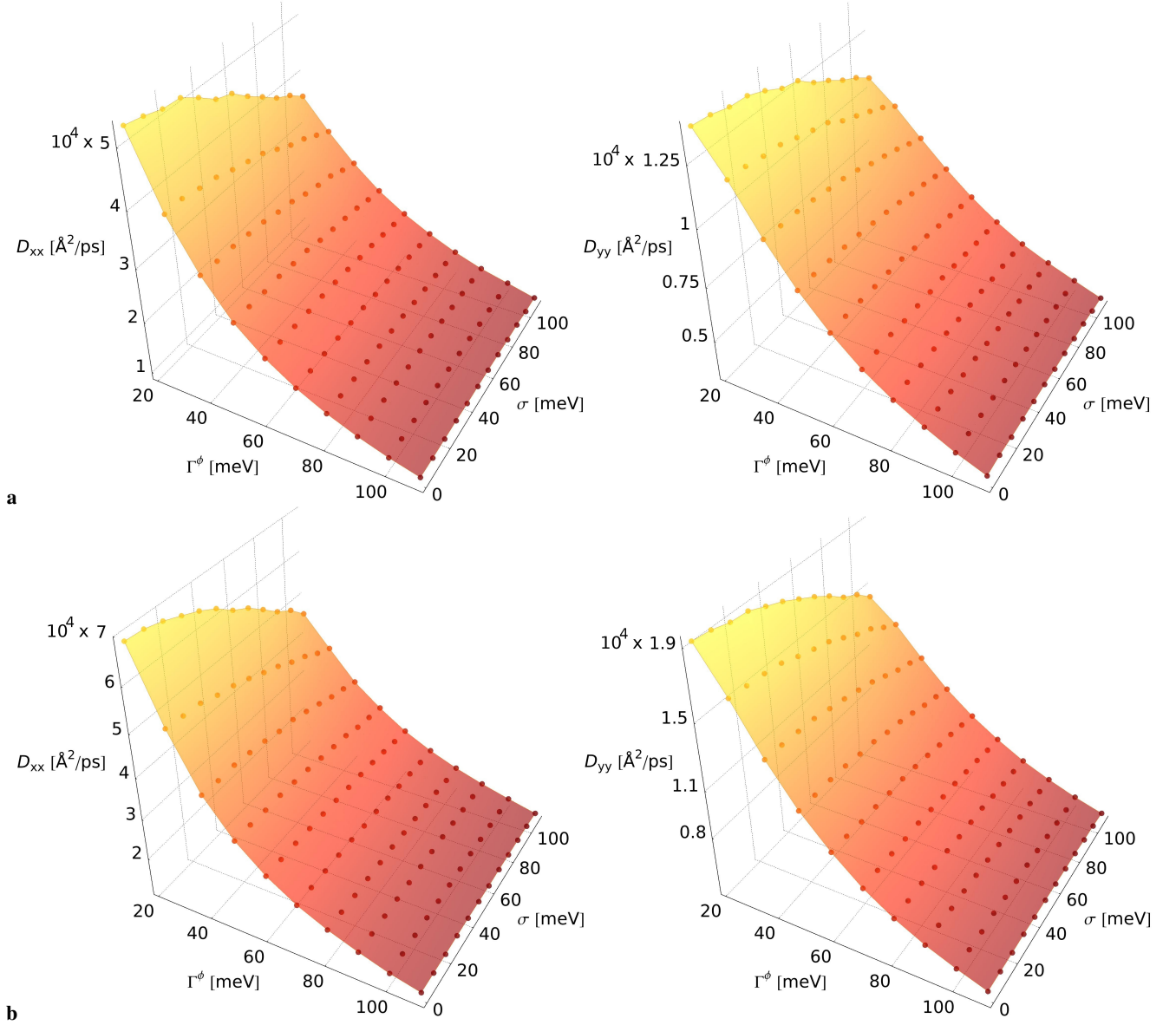


Figure 13. Diffusion coefficients of singlet excitons in 2D J-aggregates of TC (panel a) and TDBC (panel b) as functions of static  $\sigma$  and dynamic disorders  $\Gamma^\phi$ . The initial condition for propagation was injection at  $E_{in} = -281$  meV for TDBC and  $E_{in} = -287$  meV for TC. The red color corresponds to smaller diffusion while the yellow indicates larger diffusion coefficients.

bration and  $\omega_{iq}$  is the frequency of the corresponding vibrational mode. Within the visible range of the spectrum, the lowest electronic transition in fluorescent dyes has the largest oscillator strength. This transition determines the formation of a J-band in molecular aggregates. An approximation involving only the two lowest electronic states - the ground  $|g\rangle$  and the first excited  $|e\rangle$  states of a monomer - can provide good description of the excitation dynamics as long as the second excited state is far enough from the first state. This approximation has been used previously to model excitons in J-aggregates [15, 98, 99]. In the two-level approximation Eq. A1 simplifies to

$$\hat{H}_{\text{mol}} = \tilde{\Omega}_e |e\rangle\langle e| + \sum_q \omega_q \hat{b}_q^\dagger \hat{b}_q + \sum_q \kappa_q |e\rangle\langle e| \left( \hat{b}_q^\dagger + \hat{b}_q \right) \quad (\text{A2})$$

where we have assumed that the frequencies of the vibrational modes are the same for all electronic states, and the renormalized electronic transition frequency  $\tilde{\Omega}_e = \Omega_e + \sum_q \lambda_q$  involves the reorganization energies  $\lambda_q$  associated with each mode  $q$ . The exciton-vibration coupling coefficient is defined as  $\kappa_q = \lambda_q / \Delta_q$ , where the boson operators associated with different electronic states are related by  $\hat{b}_{eq} = \hat{b}_{gq} + \hat{\Delta}_q$ . In Eq. A2 all vibrational modes correspond to the electronic ground state and the corresponding ground state indices are omitted

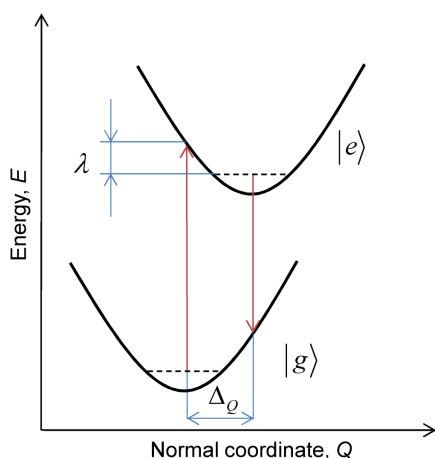


Figure 14. Schematic energy profile of a single vibrational mode in a two-level molecule.  $\lambda$  is a reorganization energy and  $\Delta_Q$  is a normal coordinate displacement.

for simplicity. The phonon creation/annihilation operator displacement  $\hat{\Delta}_q$  is related to the normal coordinate displacement operator  $\hat{\Delta}_{Qq}$  as  $\hat{\Delta}_q = \hat{\Delta}_{Qq} \cdot \sqrt{2\omega_q/\hbar}$ . A schematic

diagram of a two-level molecule is shown in Fig. 14.

## Appendix B: Exciton manifolds

For an aggregate consisting of  $N$  molecules all  $2^N - 1$  excited states can be classified into  $N$  different exciton manifolds - single exciton  $X^{(1)}$ , bi-exciton  $X^{(2)}$ , etc, see Fig. 15. The energy separation between the manifolds is of the same order of magnitude as that of the single exciton energy. The exciton manifolds are coupled by exciton relaxation or annihilation processes and also by interaction with external radiation. Within each subspace, the exciton states of monomers are coupled to each other by the Coulomb interaction, which gives rise to a resonant excitation transfer between molecules [43]. The same Coulomb interaction also renormalizes the energies of single monomer excitations. However, transitions between different exciton manifolds induced by the Coulomb interaction can be ignored. Thus, one can study single exciton dynamics by constraining the exciton space to the single exciton manifold  $X^{(1)}$  and the ground state  $X^{(0)}$ . In Fig. 15 we show a schematic diagram of exciton manifolds together with the allowed transitions for a system of three coupled molecules. Unlike molecular crystals, delocalized exciton bands are not formed in molecular aggregates due to a strong competition between the Coulomb interaction, which tends to delocalize the exciton and to the exciton-vibration coupling and structure disorder, which favor localization.

- 
- [1] E. E. Jelley, *Nature* **138**, 1009 (1936)
- [2] G. Scheibe, *Angew. Chem.* **49**, 563 (1936)
- [3] F. Würthner, T. E. Kaise, and C. R. Saha-Möller, *Angew. Chem. Int. Ed.* **50**, 3376 (2011)
- [4] D. A. Higgins, P. J. Reid, and P. F. Barbara, *J. Phys. Chem.* **100**, 1174 (1996)
- [5] K. Misawa, K. Minoshima, H. Ono, and T. Kobayashi, *Chem. Phys. Lett.* **220**, 251 (1994)
- [6] J. Moll, S. Daehne, J. R. Durrant, and D. A. Wiersma, *J. Fluoresc.* **4**, 57 (1994)
- [7] D. Möbius and H. Kuhn, *J. Appl. Phys.* **64**, 5138 (1988)
- [8] Y. Shirasaki, P. O. Anikeeva, J. R. Tischler, M. Scott Bradley, and V. Bulović, *Chem. Phys. Lett.* **485**, 243 (2010)
- [9] J. R. Tischler, G. M. Akselrod, M. S. Bradley, J. Chan, E. R. Young, D. G. Nocera, T. M. Swager, and V. Bulović, *Microsystems Technology Laboratories Annual Research Report*(2009)
- [10] H. Marciniak, X.-Q. Li, F. Würthner, and S. Lochbrunner, *J. Phys. Chem. A* **115**, 648 (2011)
- [11] A. Eisfeld and J. S. Briggs, *Chem. Phys.* **281**, 61 (2002)
- [12] P. Michetti and G. La Rocca, *Phys. Rev. B* **77**, 1 (2008)
- [13] F. C. Spano and S. Mukamel, *J. Chem. Phys.* **91**, 683 (1989)
- [14] F. C. Spano, *Acc. Chem. Res.* **43**, 429 (2010)
- [15] J. Knoester, *Phys. Rev. A* **47**, 2083 (1993)
- [16] S. T. Smiley, M. Reers, C. Mottola-Hartshorn, M. Lin, A. Chen, and T. W. Smith, *Proc. Natl. Acad. Sci.* **88**, 3671 (1991)
- [17] T. H. James, *The Theory of the Photographic Process* (Macmillan, New York, 1977)
- [18] K. Saito, *J. Phys. Chem. B* **103**, 6579 (1999)
- [19] K. Sayama, S. Tsukagoshi, K. Hara, Y. Ohga, A. Shinpou, Y. Abe, S. Suga, and H. Arakawa, *J. Phys. Chem. B* **106**, 1363 (2002)
- [20] D. Lidzey, D. Bradley, T. Virgili, a. Armitage, M. Skolnick, and S. Walker, *Phys. Rev. Lett.* **82**, 3316 (1999)
- [21] J. Bellessa, C. Bonnard, J. C. Plenet, and J. Mugnier, *Phys. Rev. Lett.* **93**, 036404 (2004)
- [22] G. Akselrod, Y. Tischler, E. Young, D. Nocera, and V. Bulovic, *Phys. Rev. B* **82**, 113106 (2010)
- [23] B. J. Walker, G. P. Nair, L. F. Marshall, V. Bulović, and M. G. Bawendi, *J. Am. Chem. Soc.* **131**, 9624 (2009)
- [24] B. J. Walker, V. Bulović, and M. G. Bawendi, *Nano Lett.* **10**, 3995 (2010)
- [25] A. Eisfeld, R. Kniprath, and J. S. Briggs, *J. Chem. Phys.* **126**, 104904 (2007)
- [26] L. D. Bakalis and J. Knoester, *J. Chem. Phys.* **106**, 6964 (1997)
- [27] A. Pugzlys, R. Augulis, P. H. M. Van Loosdrecht, C. Didraga, V. A. Malyshev, and J. Knoester, *J. Phys. Chem. B* **110**, 20268 (2006)
- [28] L. K. G. Scheibe, *Naturwissenschaften* **26**, 412 (1938)
- [29] W. J. Harrison, D. L. Mateer, and G. J. T. Tiddy, *Faraday Discuss.* **104**, 139 (1996)
- [30] W. J. Harrison, D. L. Mateer, and G. J. T. Tiddy, *J. Phys. Chem.* **100**, 2310 (1996)
- [31] H. Nakahara, K. Fukuda, D. Moebius, and H. Kuhn, *J. Phys. Chem.* **90**, 6144 (1986)
- [32] M. Bradley, J. Tischler, and V. Bulovic, *Adv. Mater.* **17**, 1881 (2005)
- [33] E. Maltsev, D. Lypenko, B. Shapiro, G. Milburn, J. Wright, M. Brusentseva, V. Berendyaev, B. Kotov, and A. V. Vannikov,

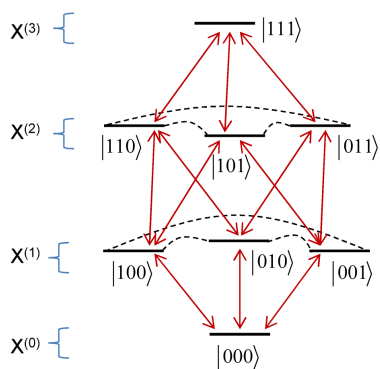


Figure 15. Schematic diagram of exciton manifolds - ground state  $X^{(0)}$ , single exciton  $X^{(1)}$ , bi-exciton  $X^{(2)}$ , and tri-exciton  $X^{(3)}$  - in an aggregate of threetwo-level molecules. The arrows between the manifolds show allowed exciton creation and relaxation transitions, and the dashed lines show Coulomb couplings between the states within a manifold. The exciton-exciton annihilation processes are shown.

- Polymer science. Series A. **42**, 299 (2000)
- [34] E. I. Maltsev, D. A. Lypenko, V. V. Bobinkin, A. R. Tameev, S. V. Kirillov, B. I. Shapiro, H. F. M. Schoo, and A. V. Vannikov, *Appl. Phys. Lett.* **81**, 3088 (2002)
- [35] J. McKeever, A. Boca, A. D. Boozer, J. R. Buck, and H. J. Kimble, *Nature* **425**, 268 (2003)
- [36] P. E. Shaw, A. Ruseckas, J. Peet, G. C. Bazan, and I. D. W. Samuel, *Adv. Funct. Mater.* **20**, 155 (2010)
- [37] B. Lyons and A. Monkman, *Phys. Rev. B* **71**, 1 (2005)
- [38] R. R. Lunt, N. C. Giebink, A. a. Belak, J. B. Benziger, and S. R. Forrest, *J. Appl. Phys.* **105**, 053711 (2009)
- [39] J. Salcedo, A. Siegman, D. Dlott, and M. Fayer, *Phys. Rev. Lett.* **41**, 131 (1978)
- [40] A. K. Ghosh and T. Feng, *J. Appl. Phys.* **49**, 5982 (1978)
- [41] V. Bulovi and S. Forrest, *Chem. Phys. Lett.* **238**, 88 (1995)
- [42] C. Madigan and V. Bulović, *Phys. Rev. Lett.* **96**, 046404 (2006)
- [43] T. Förster, "Modern quantum chemistry," (New York and London: Academic Press, 1965) Chap. Delocalized excitation and excitation transfer, pp. 93–137
- [44] H. Haken and P. Reineker, *Z. Phys.* **249**, 253 (1972)
- [45] H. Haken and G. Strobl, *Z. Phys.* **262**, 135 (1973)
- [46] P. Reineker, *Z. Phys.* **261**, 187 (1973)
- [47] V. Ern, A. Suna, Y. Tomkiewicz, P. Avakian, and R. Groff, *Phys. Rev. B* **5**, 3222 (1972)
- [48] P. Reineker, *Phys. Lett. A* **84**, 294 (1981)
- [49] V. M. Kenkre, R. Kuhne, and P. Reineker, *Z. Phys. B. Cond. Matt.* **41**, 177 (1981)
- [50] R. Kuhne, P. Reineker, and V. M. Kenkre, *Z. Phys. B. Cond. Matt.* **41**, 181 (1981)
- [51] S. Hoyer, M. Sarovar, and K. B. Whaley, *New J. Phys.* **12**, 065041 (2010)
- [52] A. S. Davydov, *Theory of Molecular Excitons* (McGraw-Hill, New York, 1962)
- [53] V. M. Agranovich and G. F. Bassani, *Electronic Excitations in Organic Based Nanostructures. Thin Films and Nanostructures, vol. 31* (Elsevier Academic Press, 2003)
- [54] D. L. Dexter, *J. Chem. Phys.* **21**, 836 (1953)
- [55] V. Czikkely, H. D. Forsterling, and H. Kuhn, *Chem. Phys. Lett.* **6**, 207 (1970)
- [56] F. Würthner, T. E. Kaiser, and C. R. Saha-Möller, *Angew. Chem. Int. Ed.* **50**, 3376 (2011)
- [57] J. Piilo, S. Maniscalco, K. Härkönen, and K.-A. Suominen, *Phys. Rev. Lett.* **100**, 180402 (2008)
- [58] P. Rebentrost, R. Chakraborty, and A. Aspuru-Guzik, *J. Chem. Phys.* **131**, 184102 (2009)
- [59] J. Roden, A. Eisfeld, W. Wolff, and W. Strunz, *Phys. Rev. Lett.* **103**, 3 (2009)
- [60] N. Gisin and I. C. Percival, *J. Phys. A: Math. Gen.* **25**, 5677 (1992)
- [61] K. Mølmer, Y. Castin, and J. Dalibard, *J. Opt. Soc. Am. B* **10**, 524 (1993)
- [62] S. Ohta, M. Nakano, R. Kishi, H. Takahashi, and S. Furukawa, *Chem. Phys. Lett.* **419**, 70 (2006)
- [63] N. G. Van Kampen, *Stochastic processes in physics and chemistry*, North-Holland personal library (Elsevier, 2007)
- [64] C. Olbrich, J. Strümpfer, K. Schulten, and U. Kleinekathöfer, *J. Phys. Chem. Lett.* **2**, 1771 (2011)
- [65] S. Shim, P. Rebentrost, S. Valteau, and A. Aspuru-Guzik, *Biophys. J.* **102** (2012)
- [66] A. Eisfeld, S. Vlaming, V. Malyshev, and J. Knoester, *Phys. Rev. Lett.* **105**, 137402 (2010)
- [67] W. H. Louisell, *Quantum Statistical Properties of Radiation* (John Wiley and Sons, 1990)
- [68] H.-P. Breuer and F. Petruccione, *The Theory of Open Quantum Systems* (Oxford University Press, New York, 2007)
- [69] T. Renger and R. A. Marcus, *J. Chem. Phys.* **116**, 9997 (2002)
- [70] A. V. Malyshev, V. A. Malyshev, and J. Knoester, *Phys. Rev. Lett.* **98**, 087401 (2007)
- [71] J. Gilmore and R. H. McKenzie, *J. Phys. Chem. A* **112**, 2162 (2008)
- [72] P. Rebentrost, M. Mohseni, I. Kassal, S. Lloyd, and A. Aspuru-Guzik, *New J. Phys.* **11**, 033003 (2009)
- [73] M. Cho, H. M. Vaswani, T. Brixner, J. Stenger, and G. R. Fleming, *J. Phys. Chem. B* **109**, 10542 (2005)
- [74] J. Adolphs and T. Renger, *Biophys. J.* **91**, 2778 (2006)
- [75] L. A. Pachón and P. Brumer, *J. Phys. Chem. Lett.* **2**, 2728 (2011)
- [76] M. B. Plenio and S. F. Huelga, *New Journal of Physics* **10**, 113019 (2008)
- [77] D. M. Coles, A. J. H. M. Meijer, W. C. Tsoi, M. D. B. Charlton, J.-S. Kim, and D. G. Lidzey, *J. Phys. Chem. A* **114**, 11920 (2010)
- [78] H. Scher and M. Lax, *Phys. Rev. B* **7**, 4491 (1973)
- [79] H. Scher and M. Lax, *Phys. Rev. B* **7**, 4502 (1973)
- [80] T. Odagaki and M. Lax, *Phys. Rev. B* **24**, 5284 (1981)
- [81] R. Kubo, *J. Phys. Soc. Jpn.* **12**, 570 (1957)
- [82] H. van Beijeren, *Rev. Mod. Phys.* **54**, 195 (1982)
- [83] R. Ahlrichs, M. Bär, M. Häser, H. Horn, and C. Kölmel, *Chem. Phys. Lett.* **162**, 165 (1989)
- [84] F. Weigend and R. Ahlrichs, *Phys. Chem. Chem. Phys.* **7**, 3297 (2005)
- [85] J. P. Perdew, M. Ernzerhof, and K. Burke, *J. Chem. Phys.* **105**, 9982 (1996)
- [86] K. Klamt and G. Schüürmann, *J. Chem. Soc. Perkin Trans. 2*, 799 (1993)
- [87] D. Rappoport and J. Hutter, "Fundamentals of time-dependent density functional theory (lecture notes in physics 837)," (Springer Berlin / Heidelberg, 2012) Chap. Excited-State Properties and Dynamics, pp. 317–336
- [88] K. Fukui, T. Yonezawa, and H. Shingu, *J. Chem. Phys.* **20**, 722 (1952)
- [89] S. S. Batsanov, *Inorg. Mater.* **37**, 871 (2001)
- [90] N. Kometani, M. Tsubonishi, T. Fujita, K. Asami, and Y. Yonewaza, *Langmuir* **17**, 578 (2001)
- [91] W. Xu and D. Akins, *J. Phys. Chem. B* **106**, 1991 (2002)

- [92] J. Wenus, S. Ceccarelli, D. G. Lidzey, A. I. Tolmachev, J. L. Slominskii, and J. L. Bricks, *Org. Electron.* **8**, 120 (2007)
- [93] M. Chachisvilis, O. Kühn, T. Pullerits, and V. Sundström, *J. Phys. Chem. B* **101**, 7275 (1997)
- [94] V. Sundström, T. Pullerits, and R. van Grondelle, *J. Phys. Chem. B* **103**, 2327 (1999)
- [95] A. Eisfeld, *Chem. Phys.* **33**, 1 (2011)
- [96] F. Caruso, S. K. Saikin, E. Solano, S. Huelga, A. Aspuru-Guzik, and M. B. Plenio, arXiv:1110.1386v1(2011)
- [97] A. N. Sokolov, S. Atahan-Evrenk, R. Mondal, H. B. Akkerman, R. S. Sanchez-Carrera, S. Granados-Focil, J. Schrier, S. C. B. Mannsfeld, A. P. Zoombelt, Z. Bao, and A. Aspuru-Guzik, *Nat. Commun.* **2**, 437 (2011)
- [98] J. Lemaistre, *J. Lumin.* **128**, 874 (2008)
- [99] J. Lemaistre, *Chem. Phys.* **333**, 186 (2007)